Electrical Conductance of Charged Nanopores

Yoav Green*

Read Online

ACCESS | Metrics & More | Article Recommendations

ABSTRACT: A nanopore's response to an electrical potential drop is characterized by its electrical conductance, $\tilde{G}$. For the last two decades, it has been thought that at low electrolyte concentrations, $\tilde{c}_0$, the conductance is concentration-independent such that $\tilde{G} \sim \tilde{c}_0^0$. It has been recently demonstrated that surface charge regulation changes the dependency to $\tilde{G} \sim \tilde{c}_0^\alpha$, whereby the slope typically takes the values $\alpha = 1/3$ or $1/2$. However, experiments have observed slopes of $2/3$ and 1 suggesting that additional mechanisms, such as convection and slip-lengths, appear. Here, we elucidate the interplay between three mechanisms: surface charge regulation, convection, and slip lengths. We show that the inclusion of convection does not change the slope, and when the effects of hydrodynamic slip are included, the slope is doubled. We show that when all effects are accounted for, α can take any value between 0 and 1 where the exact value of the slope depends on the material properties. This result is of utmost importance in designing any electro-kinetically driven nanofluidic system characterized by its conductance.
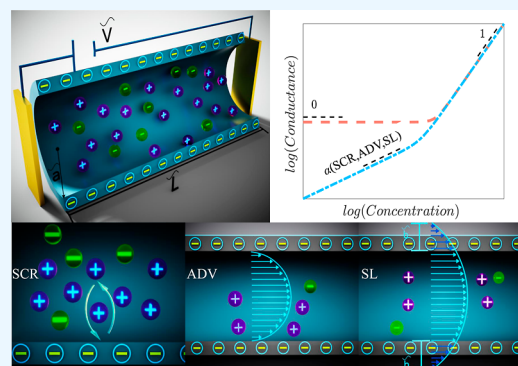
INTRODUCTION

The discovery of new materials and the development of more advanced fabrication methods result in system sizes that are ever decreasing.[1] With this comes the potential to enhance our understanding of nanoscale physics and, in parallel, revolutionize current technological setups. Of particular interest is the transport of ions across these nanoscale systems that are found in desalination[2−7] and energy-harvesting[8−21] systems, as well as biosensing,[22,23] fluid-based electrical diodes,[24−31] and various physiological phenomena.[32−35] However, numerous challenges related to scalability, fabrication technology, and the elucidation of the unknown fundamental physics at these small scales[7−9,18,36−38] remain to be overcome.

The interplay of mechanisms, unique to nanoscale systems, that determine the system's overall response, is currently not understood. Specifically, this work demonstrates how the interplay of surface charge regulation, bulk convection, and slip-length-induced convection varies the nanopore conductance. Notably, we will show that a combination of all three effects increases the slope of the conductance beyond the maximal predicted by surface charge regulation alone (this value will later be shown to be $1/2$). We will demonstrate that once all three phenomena are accounted for, the slope can take any value between 0 and 1. Notably, the model suggested in this work is free of any fitting parameters such that the response is determined solely by various system parameters.

Ohmic Conductance. The electrical conductance, $\tilde{G}$, is the ratio of the electrical current, $\tilde{I}$, to the electrical potential drop, $\tilde{V}$ (i.e. $\tilde{G} = \tilde{I}/\tilde{V}$). Stein et al.[39] demonstrated that the Ohmic conductance of nanochannels and nanopores (Figure 1a) behaved in a peculiar manner. At high bulk electrolyte concentrations, $\tilde{c}_0$, when the electric double layers (EDLs, defined below) do not overlap, the conductance is linear with the bulk concentration ($\tilde{G}_{\text{high}} \sim \tilde{c}_0$). At low bulk electrolyte concentrations, when the EDLs overlap, the conductance is given by a constant value that depends on the surface charge density, $\tilde{\sigma}_s$, and is (explicitly-) concentration-independent ($\tilde{G}_{\text{low}} \sim \tilde{c}_0^0 \sim \tilde{\sigma}_s$). The red line with squares in Figure 2 given by the well-known equation[40,41]

$$\tilde{G}_{\text{Ohmic}} = \tilde{\kappa}_{\text{cond}}\sqrt{4 + \left(\frac{\tilde{N}}{\tilde{c}_0}\right)^2}\frac{\pi\tilde{a}^2}{\tilde{L}} \tag{1}$$

depicts this behavior schematically (a detailed derivation of eq 1 can be found in ref 42). Here, $\tilde{\kappa}_{\text{cond}} = z^2\tilde{F}^2\tilde{D}\tilde{c}_0/(\tilde{R}_g\tilde{T})$ is the conductivity, $\tilde{R}_g$ is the universal gas constant, $\tilde{T}$ is the temperature, $\tilde{F}$ is Faraday's constant, $\tilde{D}$ is the diffusion
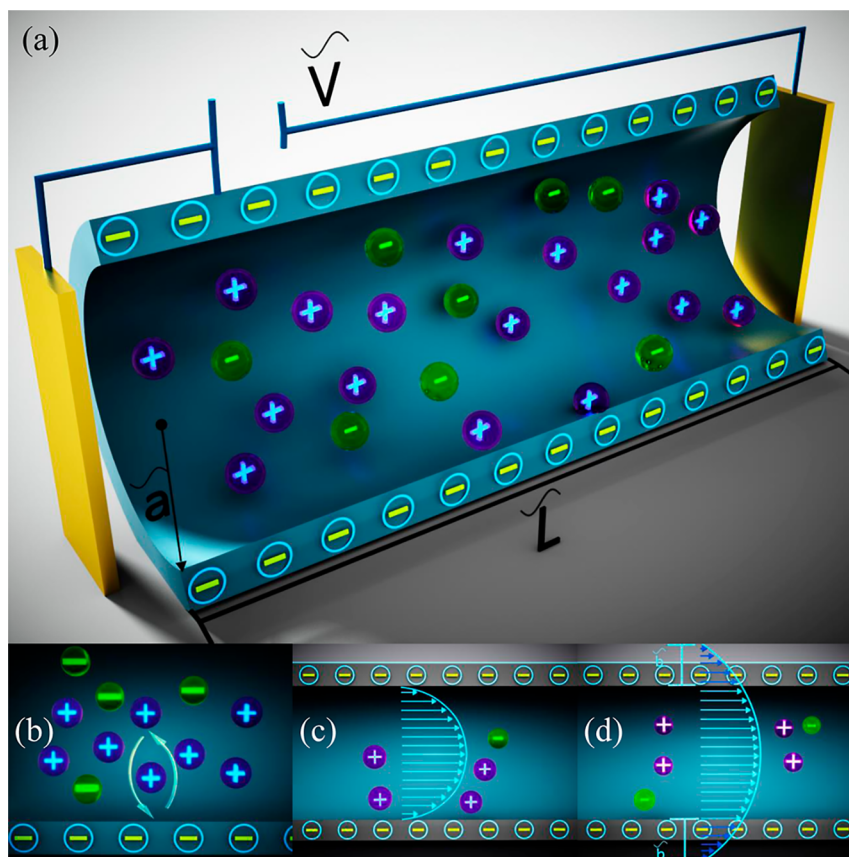
Figure 1. (a) Schematic representation of a negatively charged long nanotube ($\tilde{L} \gg \tilde{a}$) under an applied voltage, $\tilde{V}$. The negative surface charge density, $\tilde{\sigma}_s$, leads to an excess of positive counterions, represented by purple spheres, over the negative co-ions. It is assumed that the channel is highly selective ($\varepsilon = \tilde{\lambda}_D/\tilde{a} \gg 1$) which corresponds to the case of few negative ions (represented by green spheres). (b) The surface charge density is regulated by hydrogen ions, H_+, (not drawn here). (c) A schematic profile of a no-slip velocity profile. (d) A schematic velocity profile with a slip length $\tilde{b}$. Reprinted with permission from ref 42 Copyright (2022) (American Physical Society).
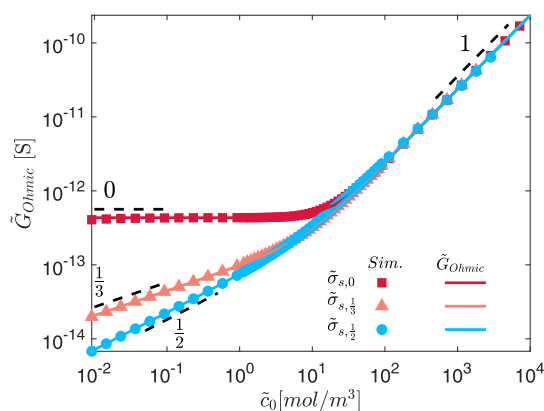

Figure 2. (a) Ohmic conductance versus concentration (eq 1) for the three surface charge densities: $\tilde{\sigma}_{s,0}$, $\tilde{\sigma}_{s,1/3}$, $\tilde{\sigma}_{s,1/2}$. Theory is denoted by lines, and simulations are denoted by markers. Details on the simulations and the values for the simulations are given in ref 42.

coefficient, and z is the valence. The pore radius and pore length are given by $\tilde{a}$ and $\tilde{L}$, respectively (Figure 1a). The average excess counterion concentration due to the surface charge density is given by $\tilde{N} = -(2\tilde{\sigma}_s)/(\tilde{a}\tilde{F}z)$. Equation 1 holds for a symmetric electrolyte where the counterion and co-ions have equal diffusion coefficients ($\tilde{D}_\pm = \tilde{D}$) and opposite valences ($z_\pm = \pm z$), and a large aspect ratio channel, $\tilde{L}/\tilde{a} \gg 1$, where all

profiles are fully-developed along. Also, the effects of convection are assumed negligible. In this work, similar to eq 1, we will consider a large aspect ratio channel ($\tilde{L}/\tilde{a} \gg 1$). In contrast to eq 1, we will also account for hydrodynamic effects (i.e., advective fluxes). Finally, note that in this work, dimensional quantities are denoted with tildes, while non-dimensional quantities are without tildes.

At high concentrations, $\tilde{N} \ll \tilde{c}_0$, the conductance is linear with the concentration, $\tilde{G}_{Ohmic,high} \sim \tilde{\kappa}_{cond} \sim \tilde{c}_0$ (Figure 2), while at low concentrations, $\tilde{N} \gg \tilde{c}_0$, the conductance

$$\tilde{G}_{Ohmic,low} = \frac{2\pi\tilde{a}}{\tilde{L}} \frac{z\tilde{F}\tilde{D}}{\tilde{R}_g\tilde{T}} |\tilde{\sigma}_s| \qquad (2)$$

is explicitly concentration-independent such that $\alpha = 0$ (Figure 2). However, it has been recently suggested that the surface charge is concentration dependent due to a surface charge regulating mechanism,[43−46] which couples the surface charge density and the bulk electrolyte such that $\tilde{\sigma}_{s,\alpha} \sim \tilde{c}_0^\alpha$. Here α is the exponent of the power-law that determines the conductance's slope. Surface charge regulation predicts three distinct expressions for the surface-charge density: (1) $\tilde{\sigma}_{s,0} = -\tilde{F}\tilde{n}/\tilde{N}_a$; (2) $\tilde{\sigma}_{s,1/3} = -(2\tilde{\varepsilon}_0\varepsilon_r\tilde{R}_g\tilde{T}z\tilde{c}_0\gamma/\beta)^{1/3}$;[43] and (3) $\tilde{\sigma}_{s,1/2} = -\left(\frac{1}{2}\tilde{a}\tilde{F}\tilde{c}_0z\gamma/\beta\right)^{1/2}$;[47] where $\tilde{\varepsilon}_0$ and ε_r are the permittivity of free space and the relative permittivity, $\tilde{N}_a$ is Avogadro's

constant, and γ and β are defined below eq 4. Insertion of these three expressions into eq 1 leads to the three curves shown in Figure 2 with the appropriate slopes of $\alpha = 0$, $1/3$ and $1/2$. All three scenarios show remarkable correspondence to direct 2D numerical simulations.[42]

RESULTS

Surface Charge Regulation. Smeets et al.[48] demonstrated that under certain experimental conditions, the electrical conductance did not saturate to a zero slope. This non-zero slope was attributed to the surface charge density's dependency on the concentration. In recent years, this mechanism has started to receive increased interest. Biesheuvel and Bazant,[44] and later others,[43,45,46,49] suggested that the regulation (Figure 1b) is through the Langmuir isotherm

$$\tilde{\sigma}_s = -\frac{\tilde{F}\tilde{n}}{\tilde{N}_a}\left[1 + 10^{pK-pH_\infty}\exp\left(-\frac{\tilde{\varphi}_s}{\tilde{\varphi}_{th}}\right)\right]^{-1} \quad (3)$$

Here, $\tilde{n}$ is the maximal number of ionizable sites per unit area, pK is the disassociation constant, pH_∞ is the pH in the bulk concentration, and $\tilde{\varphi}_{th} = \tilde{R}_g\tilde{T}/\tilde{F}z$ is the thermal potential. Notably, the surface charge density is related to the electric potential at the surface $\tilde{\varphi}_s$. At low concentrations, the surface potential is $\tilde{\varphi}_s = -\tilde{\varphi}_{th}\ln[\varepsilon^2\sigma_s(\sigma_s - 4)]$,[42] where $\varepsilon = \tilde{\lambda}_D/\tilde{a} = [(\tilde{\varepsilon}_0\tilde{\varepsilon}_r\tilde{R}_g\tilde{T})/(2\tilde{F}^2 z^2 \tilde{c}_0 \tilde{a}^2)]^{1/2}$ is the normalized Debye length [or electric double layer (EDL)], and the surface charge density has been normalized by a characteristic value $\tilde{\sigma}_d = \tilde{\varepsilon}_0\tilde{\varepsilon}_r\tilde{\varphi}_{th}/\tilde{a}$ (such that $\sigma_s = \tilde{\sigma}_s/\tilde{\sigma}_d$). Reference 42 provides a detailed derivation for $\tilde{\varphi}_s$ as well as the radial-dependent distributions for the electric potential, the concentrations, and the velocity fields in the limiting case that $\varepsilon \gg 1$. This derivation is distinctly different from that of the Debye–Hückel (DH) approximation, which typically corresponds to both small potentials and $\varepsilon \ll 1$ (see Section III.C of ref 50 for discussion on these two limits, $\varepsilon \gg 1$ and $\varepsilon \ll 1$).

Inserting $\tilde{\varphi}_s$ into eq 3 yields a third-order polynomial that determines the non-dimensional surface charge density

$$\sigma_s^3 - 4\sigma_s^2 + (\beta\varepsilon^2)^{-1}\sigma_s + (\beta\varepsilon^2)^{-1}\gamma = 0 \quad (4)$$

Here, $\beta = 10^{pK-pH_\infty}$ and $\gamma = \tilde{F}\tilde{n}/(\tilde{N}_a\tilde{\sigma}_d)$. The general solution for eq 4 is not tractable, yet three solutions are immediate. When $\beta\varepsilon^2 \ll 1$, the surface charge is concentration-independent, $\sigma_{s,0} = -\gamma$. When $\beta\varepsilon^2 \gg 1$, two concentration-dependent solutions are recovered:[42] $\sigma_{s,1/3} = -[\gamma/(\beta\varepsilon^2)]^{1/3}$ and $\sigma_{s,1/2} = -\frac{1}{2}[\gamma/(\beta\varepsilon^2)]^{1/2}$. Upon dimensionalization, these three terms recapitulate the three terms given below eq 2. Because both $\tilde{\sigma}_{s,1/3}$[43] and $\tilde{\sigma}_{s,1/2}$[44] have already been compared with experiments and shown to have excellent correspondence, we do not conduct such a comparison. Instead, here we have focused on showing that the three distinct models, given above, are derived from the same equation.

The form of eq 4 suggests that depending on the parameters γ and $\beta\varepsilon^2$, the surface charge varies continuously from one case to the other. In fact, Uematsu et al.[45] demonstrated, via numerical simulations, that the slope transitions continuously between 0 to 1/2. Uematsu et al.[45] numerically solved the 1D Poisson–Nernst–Planck equations along with the Langmuir isotherm (eq 3). They investigated how the conductance and its slope varied

with the $(pK, pH_\infty, \tilde{c}_0, \tilde{n}, \tilde{a})$ phase space. In particular, in their numerical simulations, $\tilde{a}$, $\tilde{n}$, pK were set, while pH_∞ and $\tilde{c}_0$ were scanned. They numerically calculated the conductance for each configuration in their $\tilde{c}_0 - pH$ phase space using the relation $\alpha = d(\ln \tilde{G})/d(\ln \tilde{c}_0)$. Because, they were undertaking numerical simulations, they could consider both low and high concentrations. Unexpectedly, they showed that the slope was 1 at high concentrations (as shown in Figure 2), while at low concentrations, the slope α varied from 0 to 1/2. Figure 3 shows
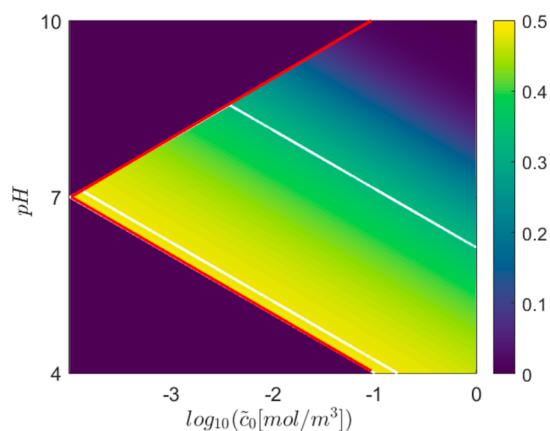

Figure 3. Color map of the slope α, in the $\tilde{c}_0 - pH$ plane of the Ohmic conductance, $\tilde{G}_{Ohmic,low}$ (eq 2). White diagonal lines denote the lines of constant slope of $\alpha = 1/3$ and $\alpha = 0.483$. Here, we have used the values of Figure 1 from ref 45: $\tilde{a} = 35$ [nm], pK = 5, and $\tilde{n} = 0.2$ [nm^{-2}] as well as their suggested cutoffs (thick red lines). Reprinted with permission from ref 42 Copyright (2022) (American Physical Society).

our recapitulation of Uematsu et al.'s[45] Figure 1 low-concentration results. We use the Newton–Raphson method to numerically evaluate eq 4 for $\tilde{\sigma}_s$. We then insert $\tilde{\sigma}_s$ into the expression for the conductance (eq 2) and calculate the slope α. The benefits of our approach are twofold. On the technical side, even though 1D finite element simulations are no longer computationally costly, scanning a 5D (or 2D) phase space can be quite burdensome. In contrast, our almost analytical approach allows one to scan any phase space to any desired resolution in an almost instantaneous manner. For example, while Uematsu et al.'s Figure 1 is pixilated, our Figure 3 is smooth. From the physical insight perspective, our approach can also rationalize Uematsu et al.'s[45] baffling observation that lines of constant slopes (and constant colors) appeared to be given by stripes. Equation 4 provides a remarkable and intuitive explanation—for a given value of γ, these are lines of constant $\beta\varepsilon^2$.[42] Thus, Figure 3 demonstrates two key results: (1) the slope varies continuously between 0 to 1/2 and (2) the slopes are lines of constant $\beta\varepsilon^2$.

Conductance with No-Slip Convection. Equation 1 holds for both high and low concentrations but no longer holds upon the inclusion of convective effects. This work focuses on the low-concentration−response, which exhibits slope variability, we emphasize that the expressions below hold only for low concentrations.

At low concentrations, the sum of the Ohmic and the no-slip advective conductance terms is (Figure 1c) is[42]

$$\tilde{G}_{total,no-slip} = \tilde{G}_{Ohmic,low} + \tilde{G}_{adv,no-slip} \quad (5)$$

where

$$\tilde{G}_{adv,no-slip} = -8\tilde{\kappa}_{cond}\varepsilon^2 Pe\left[\frac{\tilde{\sigma}_s}{\tilde{\sigma}_d} + 4\ln\left(1 - \frac{1}{4}\frac{\tilde{\sigma}_s}{\tilde{\sigma}_d}\right)\right]\frac{\pi\tilde{a}^2}{\tilde{L}} \quad (6)$$

Here, $Pe = \tilde{\varepsilon}_0\tilde{\varepsilon}_r\tilde{\varphi}_{th}^2/(\tilde{\mu}\tilde{D})$ is the Péclet number and $\tilde{\mu}$ is the fluid's viscosity. For example, for a KCl water-based electrolyte at room temperature, one finds that the Péclet number is approximately 0.45. Note that $\tilde{\kappa}_{cond}\varepsilon^2$ is independent of the concentration such that $\tilde{G}_{adv,no-slip}$, too, is also explicitly independent of the concentration. For large surface-charges, $\tilde{\sigma}_s \gg \tilde{\sigma}_d$, typical of highly selective nanochannels, the logarithmic term in eq 6 is negligible, relative to the first term, such that[42]

$$\tilde{G}_{total,no-slip} = -4\tilde{\kappa}_{cond}\varepsilon^2\frac{\tilde{\sigma}_s}{\tilde{\sigma}_d}\frac{\pi\tilde{a}^2}{\tilde{L}}(1 + 2Pe) \quad (7)$$

Observe that while the advective term results in a non-negligible increase of the conductance,[51] the slope $\tilde{G}_{total,no-slip} \sim \tilde{\sigma}_s$ does not change relative to the Ohmic conductance (eq 2). Figure 4
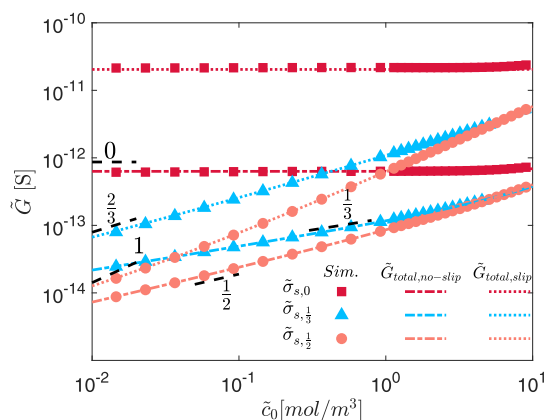

Figure 4. Conductance−concentrations curves for $\tilde{G}_{total,no-slip}$ (eq 5) and $\tilde{G}_{total,slip}$ (eq 9, with a slip length is $\tilde{b} = 10\tilde{a}$). Theory is denoted by lines, and simulations are denoted by markers. The values for the simulations are given in ref 42.

compares eq 5 to numerical simulations[42] for the three cases of $\tilde{\sigma}_{s,0}$, $\tilde{\sigma}_{s,1/3}$, and $\tilde{\sigma}_{s,1/2}$. The excellent correspondence confirms the prediction that no-slip convection does not change the slope.

Conductance with Slip Convection. The additional contribution of the slip length,[52−55] $\tilde{b}$, (Figure 1d) to the conductance is[42]

$$\tilde{G}_{adv,slip} = 4\tilde{\kappa}_{cond}\varepsilon^2 Pe\left(\frac{\tilde{\sigma}_s}{\tilde{\sigma}_d}\right)^2\frac{\tilde{b}}{\tilde{a}}\frac{\pi\tilde{a}^2}{\tilde{L}} \quad (8)$$

We add eqs 8 to 5 to get an expression for the total conductance

$$\tilde{G}_{total,slip} = \tilde{G}_{Ohmic,low} + \tilde{G}_{adv,no-slip} + \tilde{G}_{adv,slip} \quad (9)$$

Observe that $\tilde{G}_{adv,slip}$ increases the conductance and that $\tilde{G}_{adv,slip}$ scales quadratically with the surface charge ($\tilde{G}_{adv,slip} \sim \tilde{\sigma}_s^2 \sim \tilde{c}_0^{2\alpha}$). Thus, if $\tilde{G}_{total,no-slip}$ has a slope $\alpha \in [0,1/2]$ then $\tilde{G}_{total,slip}$, when dominated by $\tilde{G}_{adv,slip}$, has a slope $2\alpha \in [0,1]$.

Figure 4 compares the theoretical predictions of eq 9 to numerical simulations[42] that account for a slope length of

$\tilde{b} = 10\tilde{a}$. Figure 4 shows that when: (1) $\tilde{\sigma}_{s,0} \sim \tilde{c}_0^0$, the slope always remains $\alpha = 0$; (2) when $\tilde{\sigma}_{s,1/3} \sim \tilde{c}_0^{1/3}$, the slope transitions from $\alpha = 1/3$ to $\alpha = 2/3$; and (3) when $\tilde{\sigma}_{s,1/2} \sim \tilde{c}_0^{1/2}$, the slope transitions from $\alpha = 1/2$ to $\alpha = 1$. The excellent correspondence between simulations and theory verifies the conductance's dependency on $\tilde{\sigma}_s$ and $\tilde{b}$. Similar to $\tilde{G}_{Ohmic,low}$, which varies continuously from 0 to 1/2 (Figure 3), it can be shown that $\tilde{G}_{total,slip}$ also exhibits a continuous transition from 0 to 1 that depends on the various parameters of the system (not shown here, see ref 42). We note here that in a recent theoretical endeavor, Manghi et al.[49] derived a very similar (almost identical) expression to eq 9 (which follows from eqs 6−8). However, they have introduced several empirical terms that lack mathematical rigor and physical justification into their derivation. These issues are discussed thoroughly in ref 42. If one removes most of these empirical terms, then our eq 9, would be almost identical to eq 19 of Manghi et al.[49] However, their analysis includes several errors.[42] Thus, the novelty of this work also lies within the analysis—here, we have predicted the doubling of the slope from α to 2α for the most general scenario.

The finding that the slope doubles is of utmost experimental importance. In a recent experimental work,[56] using nanotube porins, a 2/3 slope was measured, suggesting that the effects of convection and slip are significant. Reference 56 rationalized their results using the theoretical predictions of ref 49, who predicted a slope of $\alpha = 2/3$. However, ref 49 model holds only for the specific case $\tilde{\sigma}_{s,1/3} \sim \tilde{c}_0^{1/3}$ ($\tilde{G}_{total,slip} \sim \tilde{c}_0^{2/3}$) whereby the universal solution, $\tilde{G}_{total,slip} \sim \tilde{c}_0^{2\alpha}$ [eq 9], holds for all $\alpha \in [0,1/2]$ (see ref 42 for a detailed discussion between this model and that of ref 49). The doubling of the slope from 1/2 to 1 could explain ref 3 finding that decreasing the pH from 7.5 to 3 increased the slope. This is consistent with Figure 3. Hence, the main finding of this work has been to show the doubling of the slope from α (for convection without slip, Figure 3) to 2α (for convection with slip, not shown here, see ref 42) is more robust than what was previously assumed.

■ DISCUSSION

In recent years, the characterization of the electrical conductance of nanochannels has received increased interest. This is attributed to two experimental considerations. First, while it is slightly time-consuming, it is relatively easy to measure the conductance at various concentrations and supposedly easy to interpret these results. Second, the change in the slope is an excellent indicator of when the channel achieves the high selectivity required for desalination and energy harvesting. Thus, the conductance provides the experimentalist with the required knowledge of the appropriate experimental conditions to consider. However, because of the numerous effects, interpretation of the results can be confusing. In this work, we have elucidated how the combined interplay of numerous phenomena (surface charge regulation, convection, and slip lengths) can radically change the simplest response of the nanochannel—the slope of electrical conductance as a function of the bulk concentration.

The model presented in this work is the exact solution of the fully coupled Poisson−Nernst−Planck−Stokes equation.[42,57] A minimal number of assumptions have been embedded in the model [including the assumption of a large aspect ratio ($\tilde{L} \gg \tilde{a}$)]. Direct numerical simulations of the fully coupled equations

show a remarkable correspondence and confirm the findings presented here and in an expanded work (ref 42). Namely, we have demonstrated that with surface charge regulation, the slope is not restricted to the typical three discrete values of 0, 1/3, and 1/2 but rather the slope can take any value between 0 and 1/2. The inclusion of convection alone does not change the slope, but it does enhance the conductance by a factor of twice the Péclet number (which is a value that characterizes the electrolyte). The inclusion of a slip length increases the conductance and, more importantly, doubles the slope to be twice the value dictated by surface charge regulation.

The final expression $\tilde{G}_{total,slip}$ provides the interested experimentalist a vastly enhanced framework for interpreting experimental results, and a means to fit a more accurate curve with "virtually" zero fitting parameters. If the maximal number of ionizable sites per unit area, $\tilde{n}$, and the slip length, $\tilde{b}$, are known, this model is entirely devoid of fitting parameters. If they are not known, they are easily fitted.[42] In particular, in our numerical simulations, these values are proscribed a priori, and thus from the numerical perspective, we do not have any fitting parameters.

This work serves as a stepping stone to many future works that should focus on non-trivial open questions. How does the system response change if one accounts for multiple species (that are not necessarily symmetric)? How does the response change when the assumption of a large aspect ratio ($\tilde{L} \gg \tilde{a}$) is alleviated? This last question is highly pertinent to novel 2D materials whereby $\tilde{L} \sim \tilde{a}$ or even $\tilde{L} \ll \tilde{a}$. In such a scenario, the assumption of fully-developed flows needs to be re-evaluated as well as the assumption that the slip length can vary with the ratio $\tilde{a}/\tilde{L}$.[52−55] We note that for the case of high concentrations (no EDL overlap), Yariv and Sherwood[58] showed that the system can be considered to be fully developed for $\tilde{L} \sim \tilde{a}$. However, this has yet to be shown for low-concentration (and highly selective) systems and should also be examined. This issue of fully developed profiles can also be linked to how the response of the system changes when the adjacent reservoirs are accounted. It is known that under certain conditions, the effects of access resistance and microchannel resistances are no longer non-negligible.[33,59,60] Two limitations of access resistance should be mentioned. First, if the profiles are not fully developed, how access resistance effects are manifested requires reexamination. Second, the classical access resistance is derived assuming that the pore is circular and highly isolated. However, in many circumstances, the pores are rectangular or part of arrays with a spacing of the order magnitude of the diameter. We have derived the generalization of access resistances, which we term field focusing resistances, that account for the shape of the pore and its distance to its neighbors.[16,59−61] On a different note, it has been suggested that nanopores exhibit a breakdown of electroneutrality[50,62]—this too is a highly debated topic that requires additional consideration. An expanded discussion of all these open questions is provided in ref 42. Finally, there is an increased interest in understanding the coupling of pressure and electric field driven flows on the electrical currents as well as the mass flow rates in systems comprised novel materials. Such systems can, once more, be divided into systems with large aspect ratios ($\tilde{L} \gg \tilde{a}$)[63−65] and small aspect ratios ($\tilde{L} \ll \tilde{a}$).[6,66] The approach utilized here and in other works,[42,46,47] which focuses on large aspect ratio systems, is the first step in understanding the coupling in small aspect ratio systems. Future

works should try to extend our $\tilde{L} \gg \tilde{a}$ understandings to $\tilde{L} \ll \tilde{a}$ systems.

Finally, we note the findings of this work are also immensely important to the ion-channel community. The recent book of Zheng and Trudeau[67] (and references therein) demonstrates that this community, due to the inherent complexity of such systems, is primarily dependent on complicated experiments and highly involved MD numerical simulations with little or no analytical models to lead the way. Whether or not this continuum-based model would hold for nanometric channels is questionable; however, it is very likely that this model can provide first-principle concepts that can be further considered.

In conclusion, here, we have delineated the interplay of surface charge regulation, convection, and slip lengths on the slope of the conductance. The results of this work are of immense importance when designing electro-kinetically based nanofluidics systems. Our model provides crucial insights for data interpretation. They also provide a means to reduce the number of time-consuming experiments and numerical simulations needed for the preliminary characterization of such systems.

■ AUTHOR INFORMATION

Corresponding Author

Yoav Green − *Department of Mechanical Engineering, Ben-Gurion University of the Negev, Beer-Sheva 8410501, Israel;* ● orcid.org/0000-0002-0809-6575; Email: yoavgreen@bgu.ac.il

Complete contact information is available at:
https://pubs.acs.org/10.1021/acsomega.2c02266

Notes

The author declares no competing financial interest.

■ ACKNOWLEDGMENTS

■ REFERENCES

(1) Thiruraman, J. P.; Masih Das, P.; Drndić, M. Ions and Water Dancing through Atom-Scale Holes: A Perspective toward "Size Zero". *ACS Nano* **2020**, *14*, 3736−3746.

(2) Patel, S. K.; Biesheuvel, P. M.; Elimelech, M. Energy Consumption of Brackish Water Desalination: Identifying the Sweet Spots for Electrodialysis and Reverse Osmosis. *ACS ES&T Engg* **2021**, *1*, 851.

(3) Tunuguntla, R. H.; Henley, R. Y.; Yao, Y.-C.; Pham, T. A.; Wanunu, M.; Noy, A. Enhanced Water Permeability and Tunable Ion Selectivity in Subnanometer Carbon Nanotube Porins. *Science* **2017**, *357*, 792−796.

(4) Holt, J. K.; Park, H. G.; Wang, Y.; Stadermann, M.; Artyukhin, A. B.; Grigoropoulos, C. P.; Noy, A.; Bakajin, O. Fast Mass Transport Through Sub-2-Nanometer Carbon Nanotubes. *Science* **2006**, *312*, 1034−1037.

(5) Surwade, S. P.; Smirnov, S. N.; Vlassiouk, I. V.; Unocic, R. R.; Veith, G. M.; Dai, S.; Mahurin, S. M. Water Desalination Using Nanoporous Single-Layer Graphene. *Nat. Nanotechnol.* **2015**, *10*, 459−464.

(6) Feng, J.; Graf, M.; Liu, K.; Ovchinnikov, D.; Dumcenco, D.; Heiranian, M.; Nandigana, V.; Aluru, N. R.; Kis, A.; Radenovic, A. Single-layer MoS2 nanopores as nanopower generators. *Nature* **2016**, *536*, 197−200.

(7) Chen, C.; Hu, L. Nanoscale Ion Regulation in Wood-Based Structures and Their Device Applications. *Adv. Mater.* **2021**, *33*, 2002890.

(8) Bocquet, L. Nanofluidics Coming of Age. *Nat. Mater.* **2020**, *19*, 254−256.

(9) Kavokine, N.; Netz, R. R.; Bocquet, L. Fluids at the Nanoscale: From Continuum to Subcontinuum Transport. *Annu. Rev. Fluid. Mech.* **2021**, *53*, 377.

(10) Siria, A.; Poncharal, P.; Biance, A.-L.; Fulcrand, R.; Blase, X.; Purcell, S. T.; Bocquet, L. Giant Osmotic Energy Conversion Measured in a Single Transmembrane Boron Nitride Nanotube. *Nature* **2013**, *494*, 455−458.

(11) Siria, A.; Bocquet, M.-L.; Bocquet, L. New Avenues for the Large-Scale Harvesting of Blue Energy. *Nat. Rev. Chem.* **2017**, *1*, 1−10.

(12) Hong, S.; Ming, F.; Shi, Y.; Li, R.; Kim, I. S.; Tang, C. Y.; Alshareef, H. N.; Wang, P. Two-Dimensional Ti3C2Tx MXene Membranes as Nanofluidic Osmotic Power Generators. *ACS Nano* **2019**, *13*, 8917−8925.

(13) Zhang, Z.; Yang, S.; Zhang, P.; Zhang, J.; Chen, G.; Feng, X. Mechanically Strong MXene/Kevlar Nanofiber Composite Membranes as High-Performance Nanofluidic Osmotic Power Generators. *Nat. Commun.* **2019**, *10*, 1−9.

(14) Xin, W.; Zhang, Z.; Huang, X.; Hu, Y.; Zhou, T.; Zhu, C.; Kong, X.-Y.; Jiang, L.; Wen, L. High-Performance Silk-Based Hybrid Membranes Employed for Osmotic Energy Conversion. *Nat. Commun.* **2019**, *10*, 1−10.

(15) Wu, Q.-Y.; Wang, C.; Wang, R.; Chen, C.; Gao, J.; Dai, J.; Liu, D.; Lin, Z.; Hu, L. Salinity-Gradient Power Generation with Ionized Wood Membranes. *Adv. Energy Mater.* **2020**, *10*, 1902590.

(16) Green, Y.; Edri, Y.; Yossifon, G. Asymmetry-Induced Electric Current Rectification in Permselective Systems. *Phys. Rev. E: Stat., Nonlinear, Soft Matter Phys.* **2015**, *92*, 033018.

(17) Brogioli, D. Extracting Renewable Energy from a Salinity Difference Using a Capacitor. *Phys. Rev. Lett.* **2009**, *103*, 058501.

(18) Wang, L.; Wang, Z.; Patel, S. K.; Lin, S.; Elimelech, M. Nanopore-Based Power Generation from Salinity Gradient: Why It Is Not Viable. *ACS Nano* **2021**, *15*, 4093−4107.

(19) Deka, J.; Saha, K.; Kumar, S.; Srivastava, H. K.; Raidongia, K. Electrical Power Generation from the Contrasting Interfacial Activities of Boron- and Nitrogen-Doped Reduced Graphene Oxide Membranes. *ACS Appl. Nano Mater.* **2019**, *2*, 7997−8004.

(20) Saha, K.; Deka, J.; Raidongia, K. Energy from the Nanofluidic Transport of Water through Nanochannels between Packed Silica Spheres. *ACS Appl. Nano Mater.* **2019**, *2*, 5850−5856.

(21) Neog, A. B.; Gogoi, R. K.; Dutta, T.; Raidongia, K. Electrical Actuation of Hydrophobic Bilayer Membranes of Reduced Graphene Oxide and Agar for Inducing Chemical Reactions in Microdroplets. *ACS Appl. Nano Mater.* **2020**, *3*, 6629−6635.

(22) Dematties, D.; Wen, C.; Pérez, M. D.; Zhou, D.; Zhang, S.-L. Deep Learning of Nanopore Sensing Signals Using a Bi-Path Network. *ACS Nano* **2021**, *15*, 14419−14429.

(23) Slouka, Z.; Senapati, S.; Chang, H.-C. Microfluidic Systems with Ion-Selective Membranes. *Annu. Rev. Anal. Chem.* **2014**, *7*, 317−335.

(24) Karnik, R.; Fan, R.; Yue, M.; Li, D.; Yang, P.; Majumdar, A. Electrostatic Control of Ions and Molecules in Nanofluidic Transistors. *Nano Lett.* **2005**, *5*, 943−948.

(25) Karnik, R.; Duan, C.; Castelino, K.; Daiguji, H.; Majumdar, A. Rectification of Ionic Current in a Nanofluidic Diode. *Nano Lett.* **2007**, *7*, 547−551.

(26) Vlassiouk, I.; Smirnov, S.; Siwy, Z. Nanofluidic Ionic Diodes. Comparison of Analytical and Numerical Solutions. *ACS Nano* **2008**, *2*, 1589−1602.

(27) Vlassiouk, I.; Kozel, T. R.; Siwy, Z. S. Biosensing with Nanofluidic Diodes. *J. Am. Chem. Soc.* **2009**, *131*, 8211−8220.

(28) Lucas, R. A.; Siwy, Z. S. Tunable Nanopore Arrays as the Basis for Ionic Circuits. *ACS Appl. Mater. Interfaces* **2020**, *12*, 56622−56631.

(29) Sarkadi, Z.; Fertig, D.;Ható, Z.; Valiskó, M.; Boda, D. From Nanotubes to Nanoholes: Scaling of Selectivity in Uniformly Charged Nanopores through the Dukhin Number for 1:1 Electrolytes. *J. Chem. Phys.* **2021**, *154*, 154704.

(30) Fertig, D.; Matejczyk, B.; Valiskó, M.; Gillespie, D.; Boda, D. Scaling Behavior of Bipolar Nanopore Rectification with Multivalent Ions. *J. Phys. Chem. C* **2019**, *123*, 28985−28996.

(31) Abu-Rjal, R.; Green, Y. Bipolar Nanochannels: A Systematic Approach to Asymmetric Problems. *ACS Appl. Mater. Interfaces* **2021**, *13*, 27622−27634.

(32) Qiu, Y.; Lucas, R. A.; Siwy, Z. S. Viscosity and Conductivity Tunable Diode-like Behavior for Meso- and Micropores. *J. Phys. Chem. Lett.* **2017**, *8*, 3846−3852.

(33) Alcaraz, A.; López, M. L.; Queralt-Martín, M.; Aguilella, V. M. Ion Transport in Confined Geometries below the Nanoscale: Access Resistance Dominates Protein Channel Conductance in Diluted Solutions. *ACS Nano* **2017**, *11*, 10392−10400.

(34) Queralt-Martín, M.; López, M. L.; Aguilella-Arzo, M.; Aguilella, V. M.; Alcaraz, A. Scaling Behavior of Ionic Transport in Membrane Nanochannels. *Nano Lett.* **2018**, *18*, 6604−6610.

(35) Lin, K.; Lin, C.-Y.; Polster, J. W.; Chen, Y.; Siwy, Z. S. Charge Inversion and Calcium Gating in Mixtures of Ions in Nanopores. *J. Am. Chem. Soc.* **2020**, *142*, 2925−2934.

(36) Faucher, S.; Aluru, N.; Bazant, M. Z.; Blankschtein, D.; Brozena, A. H.; Cumings, J.; Pedro de Souza, J.; Elimelech, M.; Epsztein, R.; Fourkas, J. T.; Rajan, A. G.; Kulik, H. J.; Levy, A.; Majumdar, A.; Martin, C.; McEldrew, M.; Misra, R. P.; Noy, A.; Pham, T. A.; Reed, M.; Schwegler, E.; Siwy, Z.; Wang, Y.; Strano, M. Critical Knowledge Gaps in Mass Transport through Single-Digit Nanopores: A Review and Perspective. *J. Phys. Chem. C* **2019**, *123*, 21309−21326.

(37) Park, H. B.; Kamcev, J.; Robeson, L. M.; Elimelech, M.; Freeman, B. D. Maximizing the Right Stuff: The Trade-off between Membrane Permeability and Selectivity. *Science* **2017**, *356*, No. eaab0530.

(38) Saha, K.; Deka, J.; Gogoi, R. K.; Datta, K. K. R.; Raidongia, K. Applications of Lamellar Membranes Reconstructed from Clay Mineral-Based Nanosheets: A Review. *ACS Appl. Nano Mater.* **2022**, DOI: 10.1021/acsanm.1c03207.

(39) Stein, D.; Kruithof, M.; Dekker, C. Surface-Charge-Governed Ion Transport in Nanofluidic Channels. *Phys. Rev. Lett.* **2004**, *93*, 035901.

(40) Bocquet, L.; Charlaix, E. Nanofluidics, from Bulk to Interfaces. *Chem. Soc. Rev.* **2010**, *39*, 1073.

(41) Yossifon, G.; Chang, H.-C. Changing Nanoslot Ion Flux with a Dynamic Nanocolloid Ion-Selective Filter: Secondary Overlimiting Currents Due to Nanocolloid-Nanoslot Interaction. *Phys. Rev. E: Stat., Nonlinear, Soft Matter Phys.* **2010**, *81*, 066317.

(42) Green, Y. Effects of Surface-Charge Regulation, Convection, and Slip Lengths on the Electrical Conductance of Charged Nanopores. *Phys. Rev. Fluids* **2022**, *7*, 013702.

(43) Secchi, E.; Niguès, A.; Jubin, L.; Siria, A.; Bocquet, L. Scaling Behavior for Ionic Transport and Its Fluctuations in Individual Carbon Nanotubes. *Phys. Rev. Lett.* **2016**, *116*, 154501.

(44) Biesheuvel, P. M.; Bazant, M. Z. Analysis of Ionic Conductance of Carbon Nanotubes. *Phys. Rev. E* **2016**, *94*, 050601.

(45) Uematsu, Y.; Netz, R. R.; Bocquet, L.; Bonthuis, D. J. Crossover of the Power-Law Exponent for Carbon Nanotube Conductivity as a Function of Salinity. *J. Phys. Chem. B* **2018**, *122*, 2992−2997.

(46) Green, Y. Ion Transport in Nanopores with Highly Overlapping Electric Double Layers. *J. Chem. Phys.* **2021**, *154*, 084705.

(47) Peters, P. B.; van Roij, R.; Bazant, M. Z.; Biesheuvel, P. M. Analysis of Electrolyte Transport through Charged Nanopores. *Phys. Rev. E* **2016**, *93*, 053108.

(48) Smeets, R. M. M.; Keyser, U. F.; Krapf, D.; Wu, M.-Y.; Dekker, N. H.; Dekker, C. Salt Dependence of Ion Transport and DNA Translocation through Solid-State Nanopores. *Nano Lett.* **2006**, *6*, 89−95.

(49) Manghi, M.; Palmeri, J.; Yazda, K.; Henn, F.; Jourdain, V. Role of Charge Regulation and Flow Slip in the Ionic Conductance of Nanopores: An Analytical Approach. *Phys. Rev. E* **2018**, *98*, 012605.

(50) Green, Y. Conditions for Electroneutrality Breakdown in Nanopores. *J. Chem. Phys.* **2021**, *155*, 184701.

(51) Schnitzer, O.; Yariv, E. Electric Conductance of Highly Selective Nanochannels. *Phys. Rev. E: Stat., Nonlinear, Soft Matter Phys.* **2013**, *87*, 054301.

(52) Secchi, E.; Marbach, S.; Niguès, A.; Stein, D.; Siria, A.; Bocquet, L. Massive Radius-Dependent Flow Slippage in Carbon Nanotubes. *Nature* **2016**, *537*, 210−213.

(53) Xie, Q.; Alibakhshi, M. A.; Jiao, S.; Xu, Z.; Hempel, M.; Kong, J.; Park, H. G.; Duan, C. Fast Water Transport in Graphene Nanofluidic Channels. *Nat. Nanotechnol* **2018**, *13*, 238−245.

(54) Herrero, C.; Tocci, G.; Merabia, S.; Joly, L. Fast Increase of Nanofluidic Slip in Supercooled Water: The Key Role of Dynamics. *Nanoscale* **2020**, *12*, 20396−20403.

(55) Xie, Y.; Fu, L.; Niehaus, T.; Joly, L. Liquid-Solid Slip on Charged Walls: The Dramatic Impact of Charge Distribution. *Phys. Rev. Lett.* **2020**, *125*, 014501.

(56) Yao, Y.-C.; Taqieddin, A.; Alibakhshi, M. A.; Wanunu, M.; Aluru, N. R.; Noy, A. Strong Electroosmotic Coupling Dominates Ion Conductance of 1.5 Nm Diameter Carbon Nanotube Porins. *ACS Nano* **2019**, *13*, 12851−12859.

(57) Hijnen, H. J. M.; van Daalen, J.; Smit, J. A. M. The Application of the Space-Charge Model to the Permeability Properties of Charged Microporous Membranes. *J. Colloid Interface Sci.* **1985**, *107*, 525−539.

(58) Yariv, E.; Sherwood, J. D. Application of Schwarz−Christoffel Mapping to the Analysis of Conduction through a Slot. *Proc. R. Soc. A* **2015**, *471*, 20150292.

(59) Green, Y.; Eshel, R.; Park, S.; Yossifon, G. Interplay between Nanochannel and Microchannel Resistances. *Nano Lett.* **2016**, *16*, 2744−2748.

(60) Green, Y.; Abu-Rjal, R.; Eshel, R. Electrical Resistance of Nanochannel-Microchannel Systems: An Exact Solution. *Phys. Rev. Appl.* **2020**, *14*, 014075.

(61) Sebastian, J.; Green, Y. Electrical Circuit Modelling of Nanofluidic Systems. **2022**, arXiv:2205.09437. arXiv.

(62) Noh, Y.; Aluru, N. R. Ion Transport in Electrically Imperfect Nanopores. *ACS Nano* **2020**, *14*, 10518−10526.

(63) Esfandiar, A.; Radha, B.; Wang, F. C.; Yang, Q.; Hu, S.; Garaj, S.; Nair, R. R.; Geim, A. K.; Gopinadhan, K. Size Effect in Ion Transport through Angstrom-Scale Slits. *Science* **2017**, *358*, 511−513.

(64) Mouterde, T.; Keerthi, A.; Poggioli, A. R.; Dar, S. A.; Siria, A.; Geim, A. K.; Bocquet, L.; Radha, B. Molecular Streaming and Its Voltage Control in Ångström-Scale Channels. *Nature* **2019**, *567*, 87−90.

(65) Marcotte, A.; Mouterde, T.; Niguès, A.; Siria, A.; Bocquet, L. Mechanically Activated Ionic Transport across Single-Digit Carbon Nanotubes. *Nat. Mater.* **2020**, *19*, 1057−1061.

(66) Jiang, X.; Zhao, C.; Noh, Y.; Xu, Y.; Chen, Y.; Chen, F.; Ma, L.; Ren, W.; Aluru, N. R.; Feng, J. Nonlinear Electrohydrodynamic Ion Transport in Graphene Nanopores. *Sci. Adv.* **2022**, *8*, No. eabj2510.

(67) Zheng, J.; Trudeau, M. C. *Handbook of Ion Channels*; CRC Press, 2015.